

A sampling calorimeter with warm-liquid ionization chambers

S. Plewnia^a, Th. Berghöfer^a, J. Blümer^{a,b}, P. Buchholz^c, J. Engler^a, N.O. Hashim^c,
J.R. Hörandel^{b,*}, R. Lixandru^c, J. Milke^a, W. Walkowiak^c, J. Wochele^a

^a*Institut für Kernphysik, Forschungszentrum Karlsruhe, 76021 Karlsruhe, Germany*

^b*Institut für Experimentelle Kernphysik, Universität Karlsruhe, 76021 Karlsruhe, Germany*

^c*University of Siegen, Emmy-Noether-Campus, Walter-Flex-Str. 3, 57072 Siegen, Germany*

Received 16 May 2006; received in revised form 9 July 2006; accepted 14 July 2006

Available online 15 August 2006

Abstract

An iron sampling calorimeter with warm-liquid ionization chambers has been tested at the CERN SPS in order to study the signal development and to verify the energy calibration of the hadron calorimeter in the KASCADE-Grande air shower experiment. The absolute energy calibration of the detectors is discussed. Results of the analysis of the lateral and longitudinal shower development in the calorimeter are presented and compared with results from simulations based on the GEANT/FLUKA code.

© 2006 Elsevier B.V. All rights reserved.

PACS: 29.40.Vj; 95.55.Vj

Keywords: Hadron calorimeter; Liquid ionization chambers; Tetramethylpentane

1. Introduction

The use of warm liquids in ionization chambers for calorimetry combines the advantage of liquid-filled chambers, e.g. excellent proportionality of the signal to energy deposition, large dynamic range, spatial uniformity of response, and long-term stability with the convenience of room-temperature operation [1–3]. The liquids applied exhibit electron conduction due to excess electrons at room temperature. A high mobility of such electrons $\mu_e = 93 \text{ cm}^2 \text{ V}^{-1} \text{ s}^{-1}$ has been reported in the late 1960s [4] for tetramethylsilane (TMS, $\text{Si}(\text{CH}_3)_4$) up to electric fields of about 10 kV/cm. Another example for a high-mobility liquid is tetramethylpentane (TMP, C_9H_{20}). The first application of these liquids as media in fast ionization chambers was reported about a dozen years later using TMS [5]. This stimulated the development of detectors using warm liquids as ionization medium [6–8]. Chambers filled with warm liquids are ideal detectors for the read-out of large-area calorimeters for the energy measurement of

particles in high-energy or astro-particle physics. This was demonstrated in the early 1990s with a 6 m^2 calorimeter measuring hadrons induced by cosmic rays in the atmosphere [9].

The worldwide largest installation is a hadron calorimeter [10] in the KASCADE-Grande experiment [11,12] to study secondary products generated in extensive air showers which are induced by high-energy cosmic-ray particles penetrating the atmosphere. Goal of this experiment is to explore the properties of high-energy cosmic rays in the energy region from $\approx 10^{13}$ to 10^{18} eV. The hadron data are used to study the properties of high-energy nuclear interactions in the atmosphere [13–16] and to measure properties of primary cosmic rays [17,18].

The corresponding analyses require the knowledge of the energy of incident hadrons. The absolute energy calibration of the ionization chambers is established through the measurement of the signals of minimum ionizing cosmic-ray muons. The conversion of measured energy sum in the calorimeter to the energy of the incident hadron [19] is based on simulations with the GEANT package [20] using the FLUKA92 code [21]. Goal of the present investigations is to study the signal development in the chambers for the

*Corresponding author. Tel.: +49 7247 82 4802; fax: +49 7247 82 4047.
E-mail address: hoerandel@ik.fzk.de (J.R. Hörandel).

highest energies available at test beams to complement earlier measurements at lower energies [22] and to check the calibration procedure applied.

For a direct verification at a particle beam a small calorimeter module, with a structure similar to the calorimeter of the KASCADE experiment has been set up at the CERN SPS. The detector and its operation are described in Sections 2 and 3, respectively. The key point of the physical calibration of the liquid ionization chambers is that the signal yield depends on the purity of the liquid. The corresponding procedure is discussed in Section 4. The lateral and longitudinal development of cascades in the calorimeter is investigated in Sections 5 and 6. The relation between incident particle energy and registered energy is outlined in Section 7.

2. Experimental set-up

The structure of a ionization chamber is sketched in Fig. 1. It consists of a $50 \times 50 \text{ cm}^2$ stainless-steel box (made of 1 mm thick plates), with a thickness of 1.7 cm, containing four electrodes ($25 \times 25 \text{ cm}^2$, 1 mm thick) positioned in the mid-plane of the box by ceramic spacers. The mid-electrode forms two gaps with 7 mm liquid each. A ceramic feedthrough allows to apply high voltage to the electrodes and to read out their signals independently, ensuring a fine spatial segmentation of the calorimeter. A feedback preamplifier is mounted directly on the chamber in order

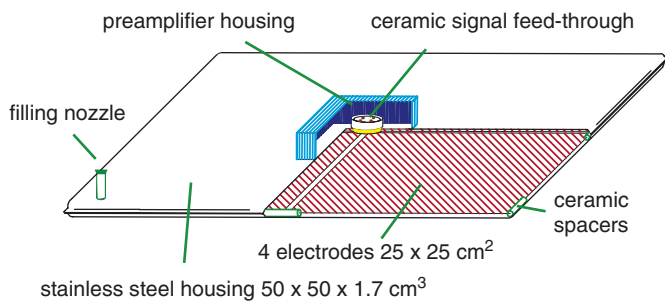


Fig. 1. Schematic view of a liquid ionization chamber.

to reduce noise pick-up. The detectors are filled with the liquid tetramethylpentane.

A set-up similar to the longitudinal structure of the KASCADE-Grande calorimeter has been chosen as sketched in Fig. 2. 60 ionization chambers are arranged in 15 layers, forming a detector with 1 m^2 active area, segmented in 16 individual read-out pads ($25 \times 25 \text{ cm}^2$) per layer. The chambers are installed in gaps of 9 cm width between the absorber slabs. A layer of chambers is installed in front and behind the absorber, respectively. The absorber consists of a lead layer (5 cm thick, corresponding to 0.3 hadronic interaction lengths λ_i or 8.9 radiation lengths X_0) followed by 13 layers of iron slabs, each 10 cm thick ($0.6 \lambda_i$ or $5.7 X_0$). The total depth amounts to $8.2 \lambda_i$. The sampling fraction of the calorimeter is about 2%.

The read-out electronics is identical to the one used in the KASCADE-Grande calorimeter [10]. A charge-integrating preamplifier is mounted directly on each chamber. The signals are transmitted to a combined main amplifier and 13-bit ADC unit with a VME-based read-out. The dynamic range of the electronics is about $1:6 \times 10^4$ [10]. For electronic calibration, a test charge was injected via a precision capacitor directly to the preamplifier of each channel.

Two plastic scintillators were installed in front of the calorimeter as trigger counters for the pion and electron runs. A third scintillator behind the calorimeter was used in dedicated runs to select muons.

3. Measurements and simulations

The calorimeter was set up at the H4 beamline of the Super Proton Synchrotron (SPS) at CERN. It was exposed to beams of protons, pions, electrons, and muons with energies between 15 and 350 GeV. Protons and pions could not be distinguished, they are treated as hadrons, as in the air shower experiment.

To identify electrons, a lead plate (15 mm thick, corresponding to $3.1 X_0$ or $0.09 \lambda_i$, not shown in Fig. 2) has been placed in front of the first layer of ionization

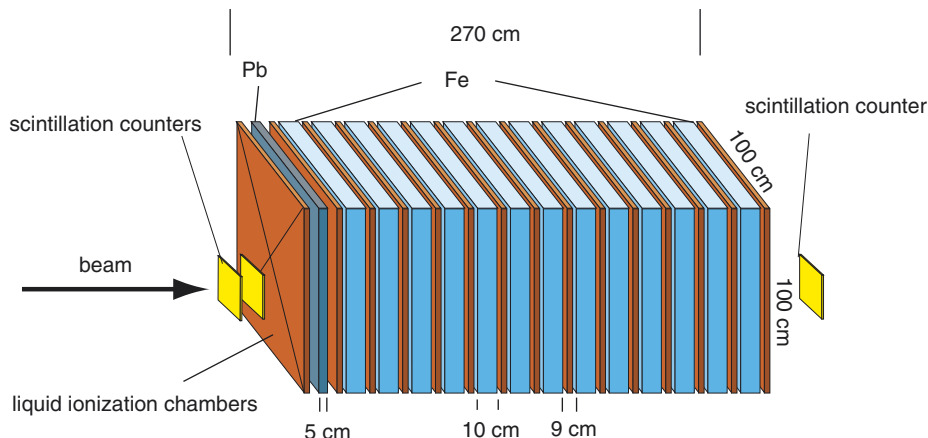


Fig. 2. Schematic view of the sampling calorimeter.

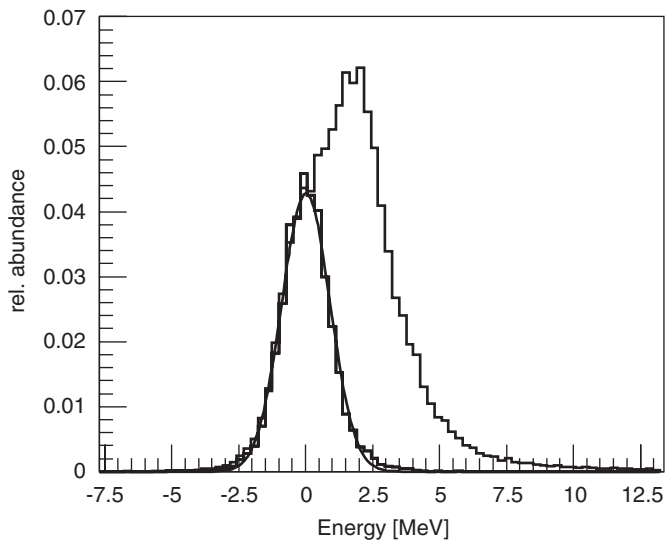


Fig. 3. Raw pulse height distribution for 50 GeV muons in a particular channel of a chamber. The distribution contains also events in which the muon passed through a neighboring pad and the response is characterized by the electronic noise which can be described by a Gaussian distribution.

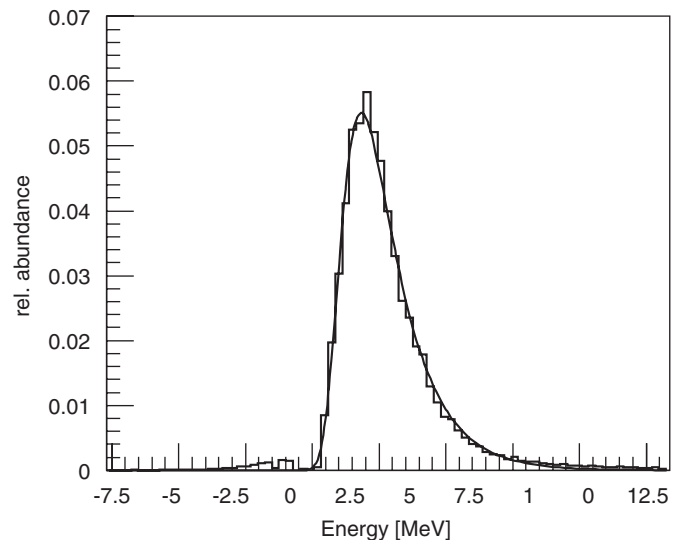


Fig. 4. Energy deposition for muons with an energy of 50 GeV in a particular channel. The curve represents a fit according to Eq. (1).

chambers and the signal in these chambers was used to select primary electrons. Selecting events with an energy deposition of more than 30 MeV or 12 minimum ionizing particles proved to be effective to reject contaminations of muons and pions in the “electron” beam.

Low-energy pions (up to 50 GeV) have been treated carefully in order to reject pions which decayed on the way to the calorimeter. In each detector layer, the beam axis hits the same pad position. For a minimum ionizing particle the energy sum would correspond to about 35 MeV. To ensure that the signal corresponds to a converted pion the energy sum has to be larger than 100 MeV.

The SPS delivers a pulsed beam. The trigger system was enabled during a spill and events were recorded. In addition, random events were taken in the time between two spills to measure the pedestal distribution in situ. These distributions exhibit a Gaussian shape with a typical width of $\sigma = 1.55$ MeV. This value corresponds to an equivalent noise charge of $3200 e^-$ or $\frac{2}{3}$ of the mean energy deposit of minimum ionizing particles.

The energy deposited in an ionization chamber by muons with an energy of 50 GeV is depicted in Fig. 3. The trigger scintillators were centered to the beam axis. For a valid trigger a particle could hit one of the four central read-out pads in each layer. Therefore, the measured pulse height distribution for an individual read-out pad, as shown in Fig. 3, contains entries for which the muon passed through the pad, as well as entries where the muon passed through a neighboring pad. To determine the fraction of the latter events, the signals of a pad in all 15 layers are summed up. In the sum distribution the muon signal is clearly separated from the pedestal. The fraction of non-muon events is obtained by a fit of two Gaussian functions to the sum distribution. A pedestal distribution

for the particular pad in question is scaled with the appropriate fraction and is shown for the example in Fig. 3. It is subtracted from the total pulse height distribution. The result is a signal distribution due to muons only, as shown in Fig. 4. The distributions are described well by a Landau distribution.

They are parameterized using the approach [23–25]

$$f(\lambda) = \frac{C}{\sqrt{2\pi}} e^{-1/2(\lambda + e^{-\lambda})} \quad (1)$$

with $\lambda = (\Delta E - E^*)/\xi$. The function gives the probability to measure an energy deposit ΔE . In the present analysis, C , E^* , and ξ are used as free parameters to include also the signal fluctuations caused by electronic noise. Typical values for muons are $E^* = 2.2$ MeV for the most probable energy and $\xi = 1.0$ MeV for the width of the distributions.

The measurements are complemented by simulations for all particle types and energies using the GEANT 3.21 package [20] with the FLUKA 92 code [21] to describe hadronic interactions.

4. Physical calibration

The absolute calibration of the measured signals can be separated into three individual steps. Firstly, an electronic calibration to determine the conversion factor from ADC values to electronic charge as described above. Secondly, a physical calibration to convert measured charge into energy deposition and finally, the conversion from energy depositions in the calorimeter to the energy of incident particles. The second step is described in this section, while the last step is discussed below in Section 7.

The measured charge Q in a chamber depends on the thickness of the active medium D , the specific ionization loss dE/dx , and the charge $G(\epsilon)$ liberated per 100 eV energy

deposit in the medium for a given electric field $\varepsilon = U/d$ as

$$Q = D \frac{dE}{dx} \frac{G(\varepsilon)}{100 \text{ eV}} f(t_d, \tau). \quad (2)$$

The function f accounts for electron charge losses. Especially at low electric fields a fraction of the liberated electrons recombines with their positive ions. Of particular interest is the contamination of the liquid with polar molecules, in particular with oxygen. Electrons are attached to a polar molecule $e^- + \text{O}_2 \rightarrow \text{O}_2^-$ and form negative ions. These have a much smaller mobility and move in the electric field with a velocity about 10^5 times slower than free electrons. Thus, the charge is not detected in fast amplifiers (integration time $2.2 \mu\text{s}$). The purity of the liquid is characterized by the average lifetime τ of free electrons. The function f for a track passing the chamber is

$$f(t_d, \tau) = \frac{\tau}{t_d} \left(1 - \frac{\tau}{t_d} \left[1 - \exp\left(-\frac{t_d}{\tau}\right) \right] \right), \quad (3)$$

where t_d is the maximum drift time in the electrode distance d . It depends as $t_d = d^2/(\mu_e U)$ on the high voltage U applied and the electron mobility in TMP $\mu_e = 29 \pm 2 \text{ cm}^2/\text{V s}$. The electrode distance d is determined for each chamber individually via capacity measurements to a precision of 1.1% [10], the nominal value is $d = 0.7 \text{ cm}$. The anode is mounted centered in the chamber and the thickness of the medium in Eq. (2) amounts to $D = 2 \cdot d$. $G(\varepsilon)$ and dE/dx are material constants, thus, the knowledge of d and τ allows an absolute energy calibration of the measured signal.

Measurements of the charge liberated in tetramethylpentane have been parameterized using a numerical approximation to Onsager's theory [26,27]. The relation

$$G(\varepsilon) = 0.678 + 5.30 \times 10^{-2} \frac{\varepsilon}{\text{kV/cm}} - 8.19 \times 10^{-4} \left(\frac{\varepsilon}{\text{kV/cm}} \right)^2 \quad (4)$$

is used for the analysis.

Values for the specific ionization loss dE/dx of passing muons have been calculated in GEANT simulations. They range from 1.41 MeV/cm at 1 GeV to 1.59 MeV/cm at 50 GeV . As can be seen from these numbers, the relativistic rise of dE/dx amounts to 12% over 1.5 decades in muon energy. This difference had to be taken into account when the muon measurements at the accelerator ($E_\mu = 50 \text{ GeV}$) are compared to calibrations with 1 GeV cosmic-ray induced muons, see below.

To determine the lifetime τ of free electrons the charge yield for passing muons as function of high voltage is measured for each chamber. An example is depicted in Fig. 5. $Q(U, \tau)$ is fitted according to Eq. (2) with τ as free parameter. In the example shown, the lifetime of the free electrons is $2.5 \pm 0.2 \mu\text{s}$. This represents a typical value, which approximately equals with the maximum drift time in a nominal chamber at 5 kV of $t_d = 3.4 \mu\text{s}$. This implies $f(t_d, \tau) \approx \frac{1}{3}$ according to Eq. (3). For an ideally pure liquid f

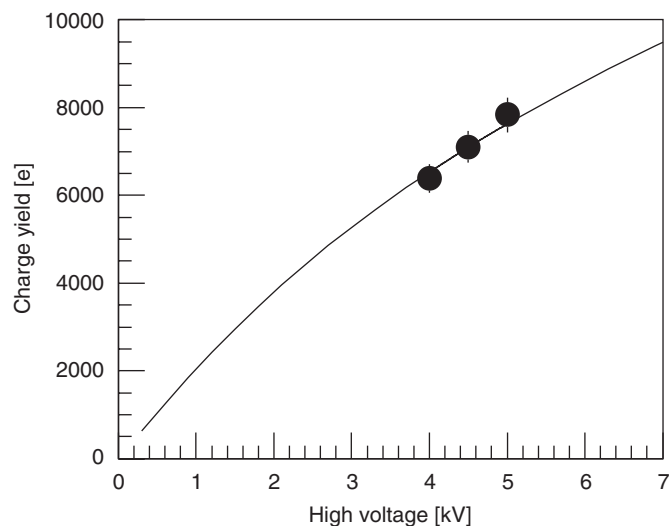


Fig. 5. Measured charge yield (in electrons) in a particular ionization chamber as function of high voltage.

reaches the value $f(t_d, \tau \rightarrow \infty) = \frac{1}{2}$, the other half of the charge is carried by the (slowly moving) ions and does not contribute to the fast signal. This implies that about $\frac{2}{3}$ of the maximum available electron signal contribute to the measured charge. This fraction could be increased by a higher electric field. However, this would also increase the risk of discharges in the chambers and augment the noise.

To check the reproducibility of these measurements the lifetimes obtained from the calibration measurements with a muon beam at the accelerator ($E_\mu = 50 \text{ GeV}$) are compared to the lifetimes obtained with the standard calibration facility at Karlsruhe. There, cosmic-ray induced muons with energies around 1 GeV are used [10]. The correlation between the two values is shown in Fig. 6. Due to the extremely non-linear dependence of f on τ , the errors increase for large lifetimes. One recognizes the good agreement between the two measurements, the mean lying exactly on the diagonal.

To determine the systematic error of the deposited energy the reproducibility of $f(t_d, \tau)$ is important. The values calculated with the lifetimes from the two measurements differ in average by about 10%. This is the error of the absolute energy scale for an *individual* channel. In the calorimeter the energy depositions of a hadron are distributed over several independent read-out channels N_{ch} situated in different layers in different ionization chambers. Since all chambers are calibrated individually, the corresponding errors of the electron life times are uncorrelated. Other systematic errors can be neglected, e.g. the systematic error of the calibration of the electronic chain has been checked repeatedly and has been found to be less than 1%. Therefore, the uncertainty of the energy of an individual hadron scales as the error of the *mean* energy deposition and, thus, is smaller by a factor $1/\sqrt{N_{\text{ch}}}$, the latter being of order of $\frac{1}{2}$. It should also be noted that average energies of cosmic-ray hadrons measured with the KASCADE calorimeter have a higher accuracy. The

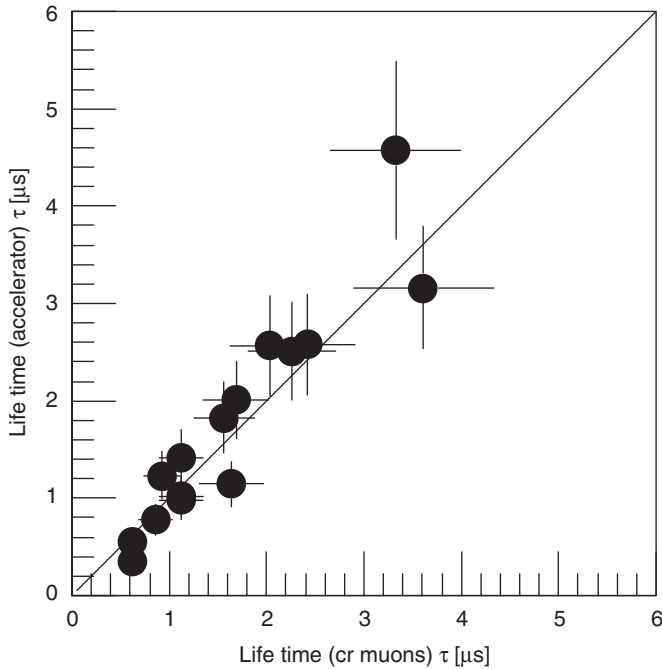


Fig. 6. Reconstructed lifetime of free electrons in the ionization liquid. Results obtained with muons at CERN are compared to measurements with cosmic-ray muons at Karlsruhe.

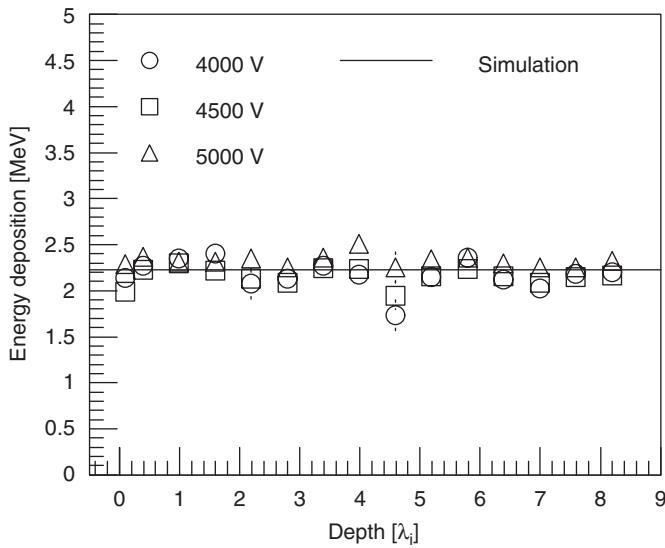


Fig. 7. Energy deposition of muons as function of depth in the calorimeter. The horizontal line indicates the value expected from simulations.

hadrons hit the calorimeter homogeneously, due to the fine lateral segmentation of the calorimeter with about 4800 channels per detector layer, the energy is deposited in independent channels. Thus, the uncertainties of the average hadron energy are smaller than for an individual hadron at a particular point of incidence and are of the order of a few (≈ 3) percent only.

How well the muon signals in the chambers are calibrated in case the electron lifetimes obtained at the accelerator are used is shown in Fig. 7 for three different

high voltages. Relatively large deviations are found for the ninth layer. For this particular chamber the signal for a minimum ionizing particle is only slightly above the noise and the signal of this chamber is not considered in the following. The average energy deposit amounts to 2.21 ± 0.1 , 2.19 ± 0.06 , and 2.33 ± 0.05 MeV for 4, 4.5, and 5 kV, respectively. The three values deviate at most by 4% from the value obtained in the simulations (2.23 ± 0.01 MeV). The mean quadratic deviations of the individual chambers from the mean values are 4.2%, 2.5%, and 2.0% for the three high voltage values, respectively. With increasing high voltage more charge is collected and the deviations decrease. For the data used in the following analyses the chambers were operated at 5 kV and the uncertainties in muon energy calibration can be taken to be about 2%.

5. Lateral distribution of energy depositions

The lateral distribution of the cascades is sampled in 16 channels per layer. In a first approximation, the distance r from the beam axis to the center of each pad is used as the position of the energy deposition. As an example, the energy deposition for 300 GeV hadrons in the fourth layer of the calorimeter is plotted in Fig. 8. One notices a strong decrease as function of distance to the beam axis and that two regions can be distinguished, which are indicated by the dashed lines. The measurements can be approximated by an exponential function with a steep slope in the inner region up to about 25 cm from the beam axis, and a flatter outer part.

The ansatz

$$\delta E(r) = C_1 \cdot \exp\left(-\frac{r}{r_1}\right) + C_2 \cdot \exp\left(-\frac{r}{r_2}\right) \quad (5)$$

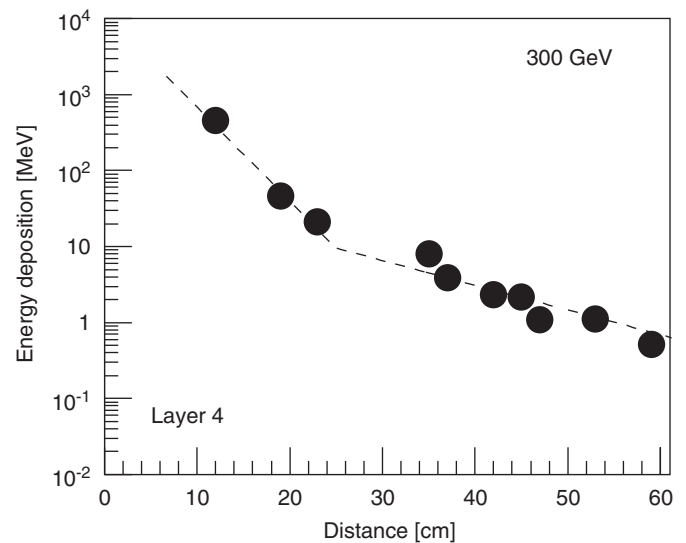


Fig. 8. Energy deposition for 300 GeV incident hadrons in a liquid ionization chamber in the fourth layer of the calorimeter as function of distance to the cascade axis. The dashed lines indicate a fall off according to two exponential functions.

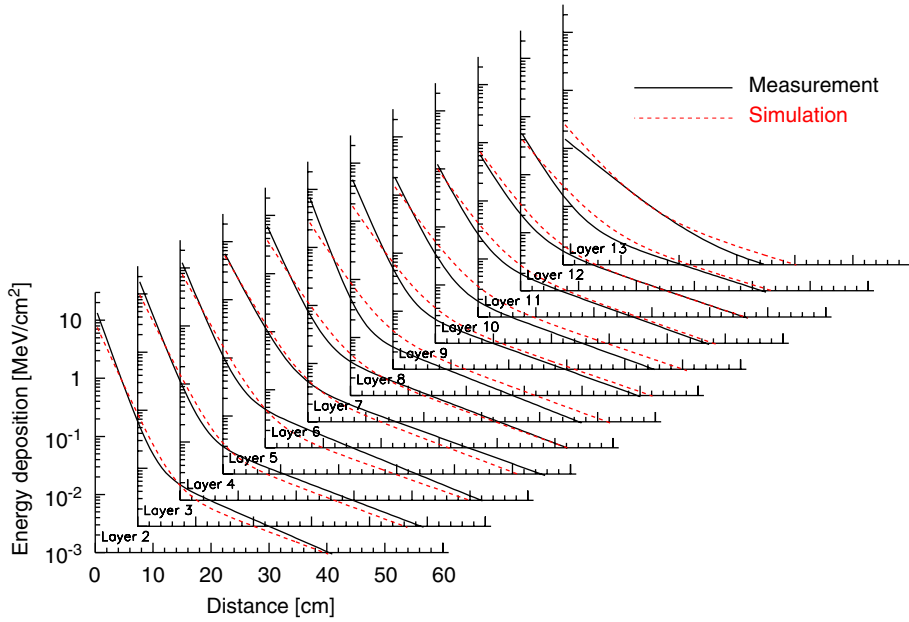


Fig. 9. Lateral distribution of the energy deposition in different layers of the calorimeter for 300 GeV hadrons. Measurements (solid lines) and simulations (dashed lines) are represented by parameterizations according to Eq. (5).

is used to approximate the energy density δE as function of the distance r to the beam axis. C_1 , C_2 , r_1 , and r_2 are fit parameters. It can be recognized that the energy deposition varies significantly within the lateral extension of a pad ($25 \times 25 \text{ cm}^2$). In the example shown, the energy deposition at 10 and 20 cm distance differ by more than a factor of 10. Hence, the approximation to assign the complete energy deposition in a pad to its geometric center is only a rough approximation. Therefore, in a fit procedure Eq. (5) has been integrated over the area of each pad

$$\Delta E = \int_{\Delta x} \int_{\Delta y} \delta E(x,y) dx dy \quad (6)$$

and the resulting energy deposition is fitted to the data, determining the values C_1 , C_2 , r_1 , and r_2 for each layer.

The result for 300 GeV hadrons is shown in Fig. 9. In the front layers the two regions with a steep and a flat fall-off can be distinguished clearly. The slope of the inner component becomes flatter with growing depth and the transition in the slope between the inner and outer component becomes less pronounced in the rear part of the calorimeter.

The energy deposition in the outer or halo region has been conjectured to be caused by low-energy neutrons which penetrate easier to these outer regions than charged particles due to their lower energy loss as compared to protons. We have studied the effect by treating the energy deposition of neutrons in the simulations separately. It turned out that they are only partly responsible for the kink and low-energy charged particles make up the halo as well [10].

The scale radii r_1 and r_2 as function of depth are summarized in Fig. 10 for hadrons with energies from 100 to 350 GeV. Both parameters increase as function of depth,

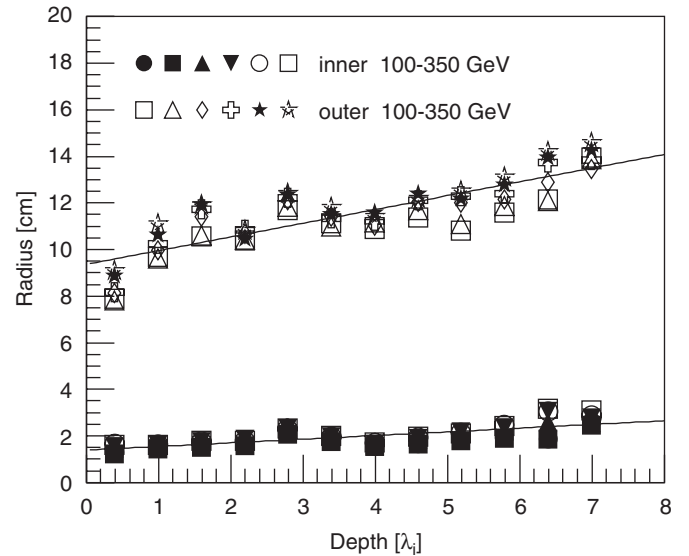


Fig. 10. Scale radii for the inner r_1 and outer r_2 component, see Eq. (5), as function of depth in the calorimeter for hadrons with energies between 100 and 350 GeV (50 GeV increment).

which illustrates that the cascades become wider when penetrating deeper into the absorber. The behavior is nearly independent of the energy. The values for the inner component range between about 1.5 and 2.5 cm, implying that the energy is extremely concentrated around the beam axis. Within the innermost 10 cm the lateral distribution falls off by a factor of almost 800 in the front layers and about 50 in the rear. The parameter r_2 varies between about 9 and 14 cm.

The results from simulations are shown in Fig. 9 as well. They reflect the overall trend of the measurements but, on a closer look, reveal also differences with respect to the

experimental values. A possible reason for the discrepancies will be discussed in the next section.

6. Longitudinal distribution of energy depositions

Integration over the lateral energy distribution yields the total energy deposit for each layer. It is shown as function of depth in the calorimeter in Fig. 11. The two summands in Eq. (5) have been integrated separately and the longitudinal development of both components is shown. In the region of the maximum, the total energy deposition is clearly dominated by the central component, while at depths exceeding six interaction lengths the outer (flatter) component becomes more important. The latter penetrates deeper into the absorber and is more weakly attenuated beyond the cascade maximum. This can be interpreted as experimental hint that this component indeed contains a large fraction of neutrons.

The data points have been fitted using the approach

$$E_{\text{dep}}(t) = A \cdot t^B \cdot \exp(-t/C) \quad (7)$$

originally introduced for electromagnetic cascades [28]. The absorber depth t is measured in interaction lengths λ_i or radiation lengths X_0 for hadrons and electrons, respectively. B characterizes the growth of the cascade before the maximum and C the exponential decrease at large depths.

The positions of the cascade maximum $t_{\text{max}} = 1/(B \cdot C)$ for the two components are shown as function of hadron energy in Fig. 12. As expected, the position of the maximum depends logarithmically on the energy for both components. Also, results of simulations are given in the figure. A reasonable agreement can be recognized for the inner component. On the other hand, in the simulations the neutron rich component penetrates about $0.5 \lambda_i$ deeper into

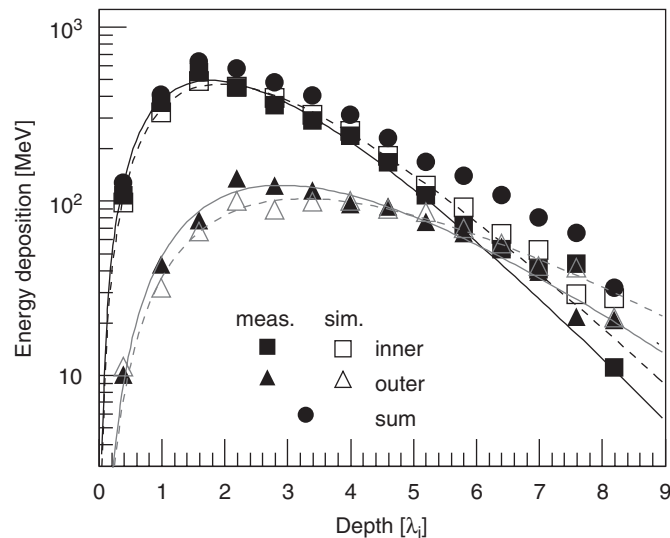


Fig. 11. Longitudinal profile of the energy deposition for 300 GeV hadrons. The contributions of the central and the outer components are shown separately. The measurements are compared to simulations. The lines indicate fits to the data according to Eq. (7).

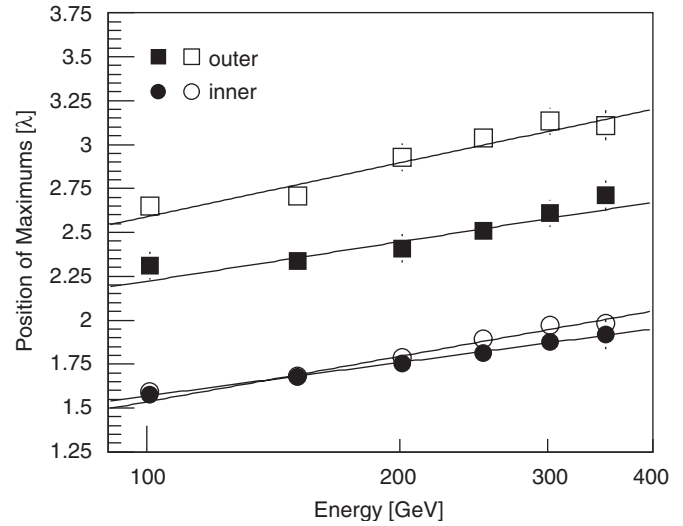


Fig. 12. Position of the cascade maximum for the two components as function of hadron energy. Measured (full symbols) and simulated (open symbols) values are shown.

the absorber as compared to the measurements. The difference is also seen in Fig. 11. This effect has been suspected already previously [10]. The separate longitudinal development curves used in the present analysis clearly show the effect. However, it should be noted that this is an interesting detail of the shower development but only a small effect for the total energy deposition. The latter is dominated by the inner component, for which a good agreement between measurements and simulations can be stated.

The total energy deposition in each layer for hadrons with energies from 30 to 350 GeV is plotted for measured and simulated cascades in Figs. 13 and 14, respectively. The lines represent fits using Eq. (7). The positions of the cascade maxima t_{max} increase logarithmically with energy for both, measurements and simulations. Good agreement is found between measurements and simulations, the increase amounts to $0.55 \lambda_i/\text{decade}$ in energy and $0.58 \lambda_i/\text{decade}$ in energy, respectively. In the figures it can be seen that the exponential decrease after the maximum is stronger in the measurements as compared to the simulations.

The attenuation length C in Eq. (7) is plotted as function of hadron energy for measured and simulated cascades in Fig. 15. For high-energy hadrons the measured attenuation length is $C = 1.1 \lambda_i$. Over the whole energy range, the measured attenuation length is about $0.3 \lambda_i$ smaller than in the FLUKA code.

The sampling of the calorimeter is optimized for hadrons and is rather coarse for electrons. Nevertheless, the response for incident electrons has been studied. The longitudinal energy depositions are shown in Fig. 16 for particles with energies from 15 to 100 GeV. Again, Eq. (7) has been used to fit the data. As can be recognized, no data points are available near the maximum of the cascades. As a consequence, the longitudinal distribution and the total

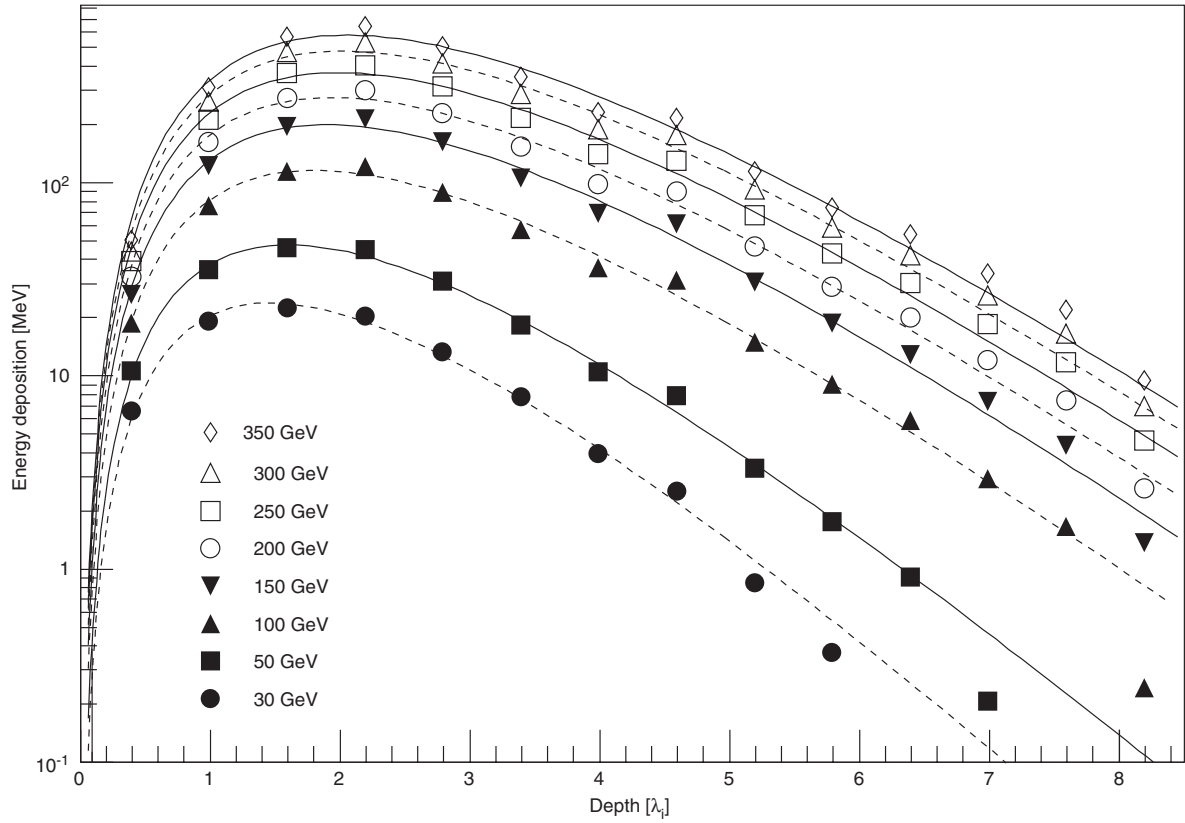


Fig. 13. Measured energy deposition as function of depth in the calorimeter for hadrons with energies from 30 to 350 GeV. The lines represent fits according to Eq. (7).

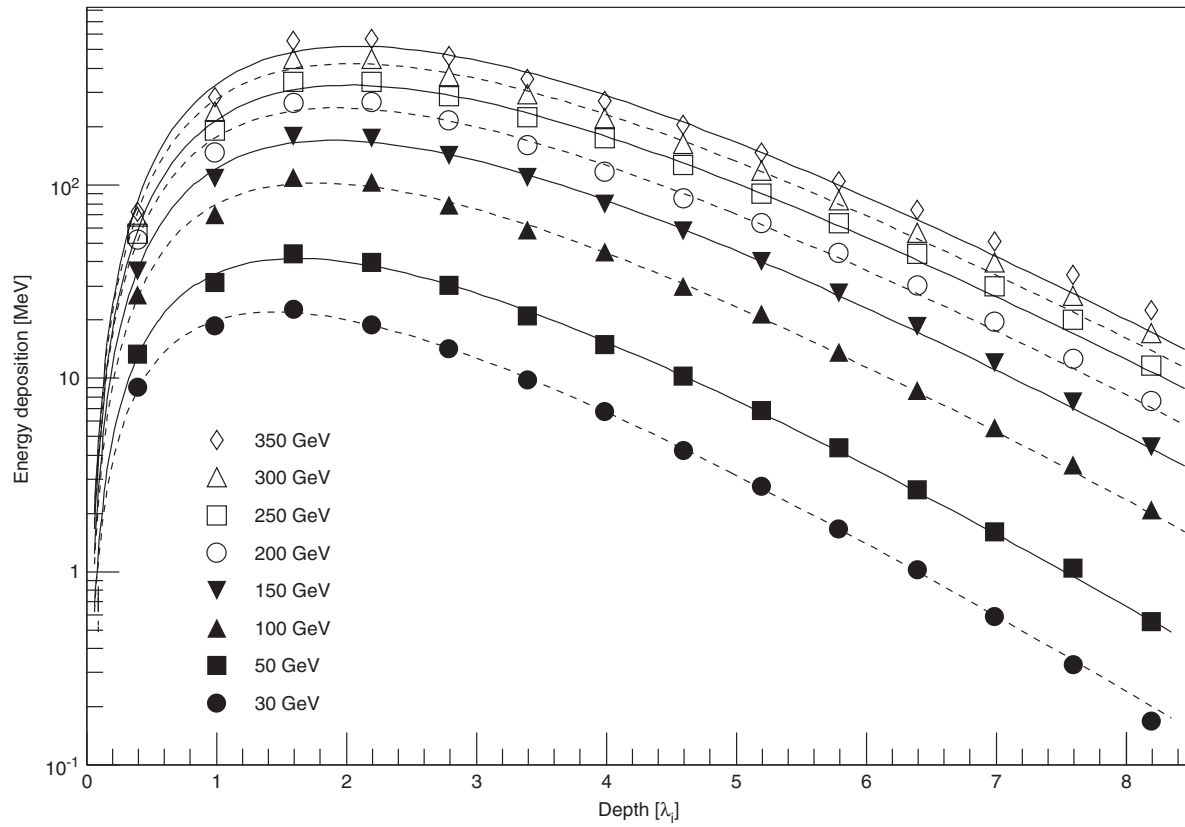


Fig. 14. Simulated energy deposition as function of depth in the calorimeter for hadrons with energies from 30 to 350 GeV. The lines represent fits according to Eq. (7).

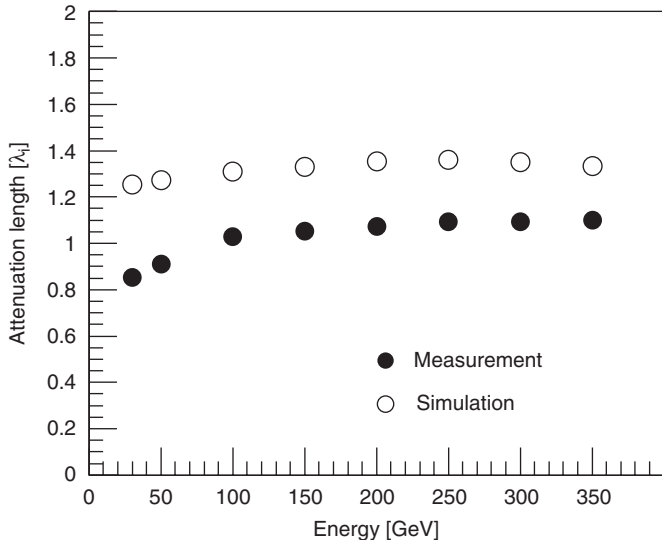


Fig. 15. Attenuation length as function of hadron energy for measured and simulated hadrons.

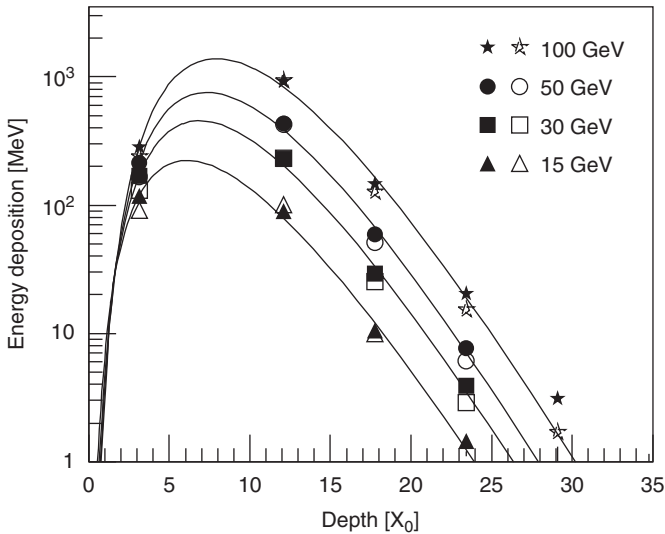


Fig. 16. Energy deposition as function of depth in the calorimeter for electrons. Shown are measurements (filled symbols) and results of simulations (open symbols). The lines represent fits to the measurements according to Eq. (7).

energy deposit in the calorimeter can be determined roughly only. Nevertheless, the measurements seem to be described rather well by the simulations, shown also in the figure. The measured attenuation length C in Eq. (7) amounts to about $1.6 X_0$ at high energies.

The depth of the maxima t_{\max} increases logarithmically with energy. The function

$$t_{\max} = X_0 \ln\left(\frac{E}{E_c}\right) \quad (8)$$

has been fitted to the measurements to determine the effective critical energy E_c and the radiation length X_0 for the lead iron absorber in combination with the air gaps.

The values $X_0 = 11.5 \pm 0.7 \text{ g/cm}^2$ and $E_c = 7.4 \pm .7 \text{ MeV}$ have been obtained. The very first layer of the calorimeter is at $3 X_0$ behind the small lead plate used to select electrons as described above, the second layer is behind the 5 cm lead absorber, i.e. up to the cascade maxima only lead absorbers are involved. But it has to be considered that Eq. (7) is fitted to the whole data set, i.e. the position of the maximum is also influenced by the presence of the iron absorbers at larger depths.

The radiation length obtained is between the literature values for iron (13.84 g/cm^2 and lead (6.37 g/cm^2) [29, p. 98]. The critical energy in solids can be approximated as $E_c = 610 \text{ MeV}/(Z + 1.24)$ [29, p. 247], yielding $E_c^{\text{Fe}} = 22.4 \text{ MeV}$ for iron and $E_c^{\text{Pb}} = 7.3 \text{ MeV}$ for lead. The effective value obtained in the present investigations is well compatible with E_c for lead.

Another interesting point is the number of electrons at shower maximum. Recently, a simple Heitler model has been used to estimate the number of electrons in air showers [30], approximating the electron number as $N_e = E/(E_c g)$. The parameter g has to be determined from measurements. Using the present results, a value of $g = 20$ is obtained, confirming the estimate of Ref. [30].

7. Integral energy sum

To reconstruct the energies of incident hadrons, the energy deposition in each layer is weighted with the amount of absorber material t_i in front of the layer, measured in interaction lengths λ_i . This procedure has to be applied for the KASCADE calorimeter due to its inhomogeneous sampling structure and is used for the present analysis as well to ensure compatibility. The resulting weighted energy sum is shown in Fig. 17. Measured values are compared to simulation results. At

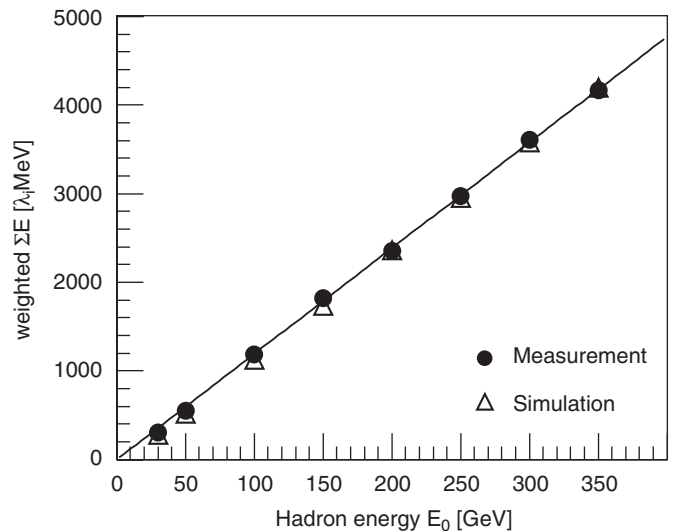


Fig. 17. Energy sum in the calorimeter as function of the incident hadron energy. The energy in each layer is weighted with the amount of absorber in front of the layer.

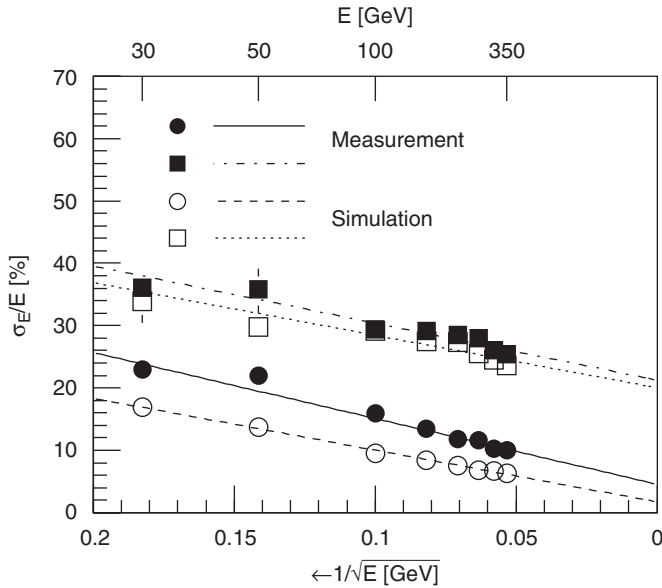


Fig. 18. Energy resolution of the calorimeter as function of hadron energy as measured and simulated. The lines represent fits according to Eq. (9). Circles are obtained taking into account all layers of the calorimeter, squares represent results, corresponding to the longitudinal segmentation of the KASCADE calorimeter.

low energies the simulations are slightly ($\sim 8\%$) below the measurements, while at high energies the deviations are smaller than 2%. For the given geometry the proportionality is $\sum E_i t_i = 7.05 \times 10^{-3} \lambda_i \cdot E_0$. Also the proportionality for electrons has been evaluated, it is given by $\sum E_i t_i = 0.104 X_0 \cdot E_0$. For this relation the absorber thickness is measured in radiation lengths.

The ratio of the total (unweighted) energy deposition for incident electrons and hadrons decreases from $e/h = 1.18$ at 30 GeV to $e/h = 1.12$ at 100 GeV. The values obtained agree well with extrapolations of earlier measurements, where the signal ratio has been investigated as function of absorber thickness using similar detectors [22]. This indicates that the calorimeter with the given sampling structure is not completely compensating. However, this is not a critical issue for the measurements of hadrons in air showers.

The RMS value σ_E of the frequency distribution of the weighted energy sum is taken as the energy resolution of the calorimeter. The relative resolution σ_E/E is plotted in Fig. 18. It improves as function of energy as $1/\sqrt{E}$ with an offset due to the finite sampling of the detector. The results obtained can be parameterized using the approach [31]

$$\frac{\sigma_E}{E} [\%] = \frac{a}{\sqrt{E[\text{GeV}]}} + b. \quad (9)$$

The values obtained are $a = 105.6 \pm 0.6$ and $b = 4.6 \pm 0.1$ for the measurements as well as $a = 83.0 \pm 1.3$ and $b = 1.7 \pm 0.1$ for the simulations. One recognizes that the fluctuations are larger in the measurements as compared to the simulations. A closer inspection of the energy sum distribution reveals that both distributions—measurement

and simulation—reveal a Gaussian shape and the mean values agree within a few percent (see also Fig. 17). However, the measured distributions are wider. A possible explanation could be that electronic noise induced by the beam broadens the distributions.

To estimate the energy resolution of the KASCADE calorimeter, only the layers corresponding to the longitudinal segmentation of this detector have been taken, yielding the values indicated by squares in the figure. Fits using Eq. (9) yield the parameters $a = 91.6 \pm 2.9$ and $b = 21.3 \pm 0.2$ for the measurements as well as $a = 84.3 \pm 8.3$ and $b = 20.0 \pm 0.6$ for the simulations. At energies exceeding 100 GeV the measured energy resolution is better than 30%, a good value for a large-area detector in a cosmic-ray experiment, measuring hadrons up to 25 TeV energy. It should be noted that these numbers give an estimate only for two reasons: The sampling structure is not exactly identical for both devices and secondly, the KASCADE calorimeter is $11 \lambda_i$ deep and therefore has a better resolution at high energies.

8. Conclusion

A sampling calorimeter equipped with warm-liquid ionization chambers has been exposed to beams of muons, electrons, pions, and protons with energies from 15 to 350 GeV at the CERN SPS. Lateral and longitudinal distributions of energy depositions in the calorimeter have been studied. The measured lateral distributions consist of two components, a central component up to a distance of 25 cm from the cascade axis and an outer component. The latter seems to be dominated by low-energy neutrons. The longitudinal behavior of the central component is well described by the GEANT/FLUKA code. On the other hand, the measured attenuation of the outer component is stronger as anticipated in the simulation code.

The results show that the absolute signal calibration of liquid ionization chambers can be based on measurements of cosmic-ray muons. The calibration constants depend on the purity of the ionization liquid, which is characterized by the mean lifetime of free electrons in the liquid.

The energy reconstruction of the KASCADE hadron calorimeter is based on simulations using the GEANT and FLUKA codes. The calibration has been confirmed up to 350 GeV by the presented accelerator measurements. At high energies the deviations between measurements and simulations amount to 2%. The systematic error of the absolute energy scale for an individual channel is dominated by the uncertainties of the lifetime of the free electrons in the liquid and amounts to about 10%. The absolute scale of the energy deposition of an individual hadron can be determined with an uncertainty of about 5%, while the average energy of many hadrons, homogeneously hitting the calorimeter has an error of a few (≈ 3) percent only.

Acknowledgments

We would like to thank all colleagues at CERN who made this work possible, in particular I. Efthymiopoulos, M. Hauschild, and L. Linssen. We acknowledge the valuable technical contributions by N. Bechtold, H. Bolz, W. Paulus, and M. Riegel of the Forschungszentrum Karlsruhe.

References

- [1] J. Engler, *J. Phys.* 22 (1996) 1.
- [2] J. Feltse, *Nucl. Instr. and Meth. A* 283 (1989) 375.
- [3] T. Virdee, *Nucl. Instr. and Meth. A* 323 (1992) 22.
- [4] W. Schmidt, A. Allen, *J. Chem. Phys.* 50 (1969) 5037.
- [5] J. Engler, H. Keim, *Nucl. Instr. and Meth. A* 223 (1984) 47.
- [6] J. Engler, et al., *Nucl. Instr. and Meth. A* 252 (1986) 29.
- [7] J. Engler, et al., *Nucl. Instr. and Meth. A* 254 (1987) 311.
- [8] M. Albrow, et al., *Nucl. Instr. and Meth. A* 265 (1988) 303.
- [9] H. Mielke, et al., *Nucl. Instr. and Meth. A* 360 (1995) 367.
- [10] J. Engler, et al., *Nucl. Instr. and Meth. A* 427 (1999) 528.
- [11] T. Antoni, et al., *Nucl. Instr. and Meth. A* 513 (2003) 490.
- [12] G. Navarra, et al., *Nucl. Instr. and Meth. A* 518 (2004) 207.
- [13] T. Antoni, et al., *J. Phys. G* 25 (1999) 2161.
- [14] T. Antoni, et al., *Astropart. Phys.* 14 (2001) 245.
- [15] T. Antoni, et al., *J. Phys. G* 27 (2001) 1785.
- [16] T. Antoni, et al., *Phys. Rev. D* 71 (2005) 072002.
- [17] T. Antoni, et al., *Astropart. Phys.* 16 (2002) 245.
- [18] T. Antoni, et al., *Astrophys. J.* 612 (2004) 914.
- [19] J. Milke, et al., in: G. Barreira, B. Tome (Eds.), *Calorimetry in High Energy Physics*, World Scientific, Singapore, 2000, p. 803 (ISBN 981-02-4304-9).
- [20] Geant 3.21 detector description and simulation tool, CERN Program Library Long Writeup W5013, CERN, 1993.
- [21] P. Aarnio, et al., *Fluka user's guide*, Technical Report TIS-RP-190, CERN, 1990.
- [22] J. Engler, et al., *Nucl. Instr. and Meth. A* 320 (1992) 460.
- [23] J.E. Moyal, *Philos. Mag.* 46 (1955) 263.
- [24] F. Sauli, *Principles of operation of multiwire proportional and drift chambers*, CERN Report 77-09, CERN, Geneva, 1977.
- [25] C. Grupen, *Particle Detectors*, Cambridge University Press, Cambridge, 1996.
- [26] L. Onsager, *Phys. Rev.* 54 (1938) 554.
- [27] G.R. Freeman, *J. Chem. Phys.* 39 (1963) 1580.
- [28] E. Longo, I. Sestili, *Nucl. Instr. and Meth.* 128 (1975) 283.
- [29] S. Eidelman, et al., *Phys. Lett. B* 592 (2004) 1.
- [30] J. Matthews, *Astropart. Phys.* 22 (2005) 387.
- [31] R. Wigmans, *Calorimetry—Energy Measurement in Particle Physics*, Oxford University Press, Oxford, 2000.